Opto-Electronic Engineering

Article

2017, Vol 44, Issue 1

All-dielectric metasurface beam deflector at the visible frequencies

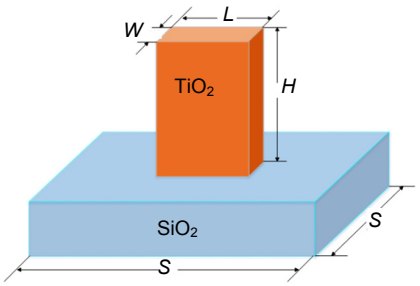

Daopeng Wang, Qingbin Fan, Jiaxing Wang, Zijie Zhang, Yuzhang Liang and Ting Xu*

National Laboratory of Solid State Microstructures, College of Engineering and Applied Sciences and Collaborative Innovation Center of Advanced Microstructures, Nanjing University, Nanjing 210093, China

Abstract: Beam deflectors are important optical elements which can control the propagation direction of the beam in free space. However, with the development of miniaturization of the optical systems, conventional reflector-based mechanical beam deflectors confront a huge challenge due to their large sizes and incompatibility to the device integration. Here we propose an all-dielectric flat metasurface beam deflector which is composed of a single layer array of TiO_2 nanoantennas resting on a fused-silica substrate. Numerical simulations are performed to demonstrate that the proposed deflectors are able to efficiently deflect the incident beam for different angles with transmission efficiency higher than 80% at visible frequencies. This ultrathin all-dielectric metasurface deflector may have great potential applications in integrated optics.

Keywords: metasurfaces; beam deflector; nanoantenna; integrated optics

DOI: 10.3969/j.issn.1003-501X.2017.01.012 **Citation:** *Opto-Elec Eng*, 2017, **44**(1): 103–107

1 Introduction

Beam deflectors are basic optical elements which can control the propagation direction of the beam in free space and play important roles in many optical systems. The traditional mechanical beam deflectors are based on the combination of mirror reflectors which make the system complex and bulky. A few years ago, several thin-film plasmonic beam deflectors using metallic nanoslits was proposed[1-2]. Limited by the strong ohmic damping caused by surface plasmon polaritons (SPPs) at the interface between metal and dielectric medium, the plasmonic beam deflectors have low transmission efficiencies at specific deflection angle, typically lower than 50%.

Recently, metasurfaces, also known as two-dimensional metamaterials, have attracted significant attentions due to their ultrathin thickness and efficient controlling of amplitude, phase and polarization of beams [3-5]. According to Huygens principle, the electromagnetic metasurfaces can be designed to achieve arbitrary wavefront. Due to the remarkable ability of full 2π phase control, metasurfaces are widely used in lensing[7-10], holograms[11-14], wave plates[15] and other applications[16-21]. In previous studies, metasurfaces are mainly designed using metallic resonant structures. Although metasurfaces using metallic resonant structures showed good behaviors in near-infrared wavelengths proposed in previous studies, their efficiencies in low band of visible wavelengths remain dissatisfactory[6, 22,-23]. To overcome the loss issue, metasurfaces using dielectrics, such as silicon[21] and titanium dioxide (TiO_2)[24], are proposed and employed in novel optical devices. For example, metalenses with high-aspect-ratio TiO_2 metasurface are designed and demonstrated in visible wavelengths, which exhibit great imaging performances including their high numerical apertures (NA) and high transmission efficiencies[24].

In this paper, all-dielectric metasurfaces composed of TiO_2 nanoantennas, which are able to efficiently manipulate the phase of incident light, are proposed to implement the deflection of visible light. As numerical demonstrations, we design several metasurface beam deflectors with deflection angles of 15°, 30°, 45° and perform finite-difference time-domain(FDTD) simulations. At visible wavelengths of 450 nm, 532 nm and 633 nm, the all-dielectric metasurface beam deflectors exhibit accurate deflection performances with transmission efficiencies more than 80%, which are higher than previously reported metal-based metasurface devices[25-28]. This all-dielectric metasurface beam deflector may have po-

Received 12 October 2016; accepted 30 December, 2016
* E-mail: xuting@nju.edu.cn

tential applications in manipulating light propagation in high-integration optical systems.

2 Principle and design

Fig. 1(a) shows the schematic diagram of the unit cell structure, consisting of a cuboid TiO_2 nanoantenna and a square SiO_2 substrate. Here, we use TiO_2 as the constitution material of the nanoantenna because TiO_2 has high refractive index, low surface roughness and very low loss in the visible-light region. The length along x, y and z-axes of TiO_2 nanoantenna are defined as L, W and H, respectively, while the period of the unit cell is S. As shown in Fig. 1(b), the TiO_2 nanoantenna can rotate with an orientation angle θ to produce a different phase delay. Here, the TiO_2 nanoantennas are considered as birefringent elements and the Jones transfer matrix can be used to model electrometric response of each TiO_2 nanoantenna. If the nanoantenna rotation angle θ=0, the Jones matrix $\boldsymbol{J}_0$ has the form

$$\boldsymbol{J}_0 = \begin{bmatrix} t_x & 0 \\ 0 & t_y e^{i\varphi} \end{bmatrix}, \tag{1}$$

where t_x and t_y are the transmission coefficients of incident light with polarization parallel to x and y-axes, respectively, and φ is the phase retardation between x and y-components. Applying the optical rotation matrix on the Jones matrix, we can get a new transfer matrix $\boldsymbol{T}$[28].

$$\begin{aligned} \boldsymbol{T} &= \boldsymbol{R}(-\theta)\boldsymbol{J}_0\boldsymbol{R}(\theta) = \\ &\begin{bmatrix} \cos\theta & -\sin\theta \\ \sin\theta & \cos\theta \end{bmatrix}\begin{bmatrix} t_x & 0 \\ 0 & t_y e^{i\varphi} \end{bmatrix}\begin{bmatrix} \cos\theta & \sin\theta \\ -\sin\theta & \cos\theta \end{bmatrix} = \\ &\frac{1}{2}(t_x + t_y e^{i\varphi})\begin{bmatrix} 1 & 0 \\ 0 & 1 \end{bmatrix} + \\ &\frac{1}{2}(t_x - t_y e^{i\varphi})\begin{bmatrix} \cos 2\theta & \sin 2\theta \\ \sin 2\theta & -\cos 2\theta \end{bmatrix}. \end{aligned} \tag{2}$$

For the incident light with polarization $|E_{in}\rangle$, calculated by the transfer matrix $\boldsymbol{T}$, the output electric field is [8, 29-30]

$$\begin{aligned} |E_{out}\rangle = \boldsymbol{T}|E_{in}\rangle &= \frac{1}{2}(t_x + t_y e^{i\varphi})|E_{in}\rangle + \\ &\frac{1}{2}(t_x - t_y e^{i\varphi})[\langle E_{in}|R\rangle e^{-i2\theta}|L\rangle + \langle E_{in}|L\rangle e^{i2\theta}|R\rangle], \end{aligned} \tag{3}$$

where $\langle E_{in}|R\rangle$ and $\langle E_{in}|L\rangle$ denote inner products. In case of t_x=t_y =1, φ=π and the incident light with $|L\rangle$ state, the output field develops into

$$|E_{out}\rangle = e^{i2\theta}|R\rangle. \tag{4}$$

From Eq.(4) we can get the relationship between the phase shift $\Delta\varphi$ and the rotate angle θ:

$$\Delta\varphi = 2\theta, \tag{5}$$

For the left-circularly polarized (LCP) and right-circularly polarized (RCP) incident light, $[(t_x - t_y e^{i\varphi})/2]^2$ is defined as the polarization conversion efficiency (PCE). We can infer that when t_x=t_y =1 and φ=π, the PCE equals to 100% and phase shift of the light passing through the nanoantennas satisfies Eq. (5), which indicates the phase shift of incident light can be controlled by rotating the nanoantenna.

To implement deflection of light at a specific angle α, the phase profile $\Delta\varphi(x)$ of the deflector at position x should take the form [1]

$$\Delta\varphi(x) = 2n\pi + \Delta\varphi(0) - (2\pi/\lambda)\cdot x\cdot\sin\alpha, \tag{6}$$

where n is an integer, x is the x-coordinate of the nanoantenna, $\Delta\varphi(0)$ is the phase profile at x=0 and we assume the rotation angle θ=0 at this position, and λ is the free-space wavelength.

According to Eq.(5) and Eq.(6), in order to realize the deflection function for an angle α, $\Delta\varphi(x)$–$\Delta\varphi(0)$ should satisfy the relationship 2θ=$\Delta\varphi(x)$–$\Delta\varphi(0)$, and each nanoantenna should be rotated by an angle

$$\theta = n\pi - (\pi/\lambda)\cdot x\cdot\sin\alpha. \tag{7}$$

Therefore, the key point to manipulate deflection is to determine the structural parameters and positions of the nanoantennas.

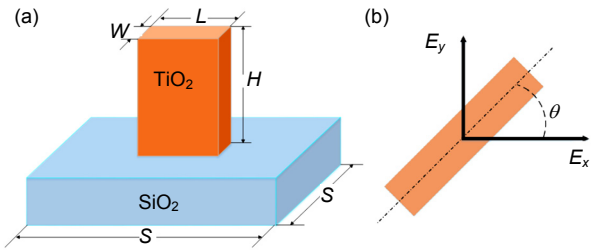

Fig.1 (a) Front view of the beam deflector unit cell, showing unit cell periodicity S, nanoantenna width W, length L and height H. At the wavelength of 450 nm, S=230 nm, L=145 nm, W=60 nm, H=500 nm; At the wavelength of 532 nm, S=270 nm, L=210 nm, W=70 nm, H=550 nm; At the wavelength of 633 nm, S=320 nm, L=270 nm, W=105 nm, H=600 nm. (b) Cross-section of single nanoantenna with rotation angle θ.

3 Simulation and discussion

To evaluate PCE, a nanoantenna unit cell with periodic boundary condition is simulated by finite-difference time-domain (FDTD) method. A LCP beam passes through the SiO_2 substrate, and then is modulated by the TiO_2 nanoantennas array. The parameters (n-k) of TiO_2 are taken from reference [31]. Three nanoantennas operating at different wavelength ranges are designed with the following structural parameters: nanoantenna 1: S=230 nm, L=145 nm, W= 60 nm, H=500 nm; nanoantenna 2: S=270 nm, L=210 nm, W=70 nm, H=550 nm; nanoantenna 3: S=320 nm, L=270 nm, W=105 nm, H=600 nm. As shown in Fig.2, the PCEs of three different nanoantennas are all higher than 90%, and the PCE of each structural parameter at the wavelengths of 450 nm, 532 nm and 633 nm is 94.1%, 94.3% and 91.3%,

respectively, indicating that the LCP light is almost completely converted into RCP light. The dips in PCE simulation results are caused by the magnetic and electric resonances and they can hardly have influence on the deflection behaviors as they are far away from the chosen operation wavelengths. The simulation results of PCE are well consistent with the theoretical expectation.

Next, the full-wave FDTD simulations with a boundary of perfect matched layers (PML) are employed to calculate the near-field and far-field electromagnetic responses of the metasurface deflectors. The simulated near-field phase distributions of electric field corresponding to deflectors designed for the angles of 15°, 30° and 45° at three wavelengths of 450 nm, 532 nm and 633 nm are shown in Figs. 3(a)~3(c). It can be obviously observed that the deflections take place after the incident light passing through the TiO_2 nanoantennas array. The corresponding deflected angles are around 15°, 30° and 45°, respectively, which is coincident well with the theoretical design angle. It is worth mentioning that a symmetrical result (deflect to the other direction with the same angle) could be achieved under the incidence of a RCP light.

Figs. 4(a)~4(c) present the normalized far-field transmitted power distributions as a function of deflection angle. As expected, the highest peaks of the spectra which represent the deflection angles are located at the angles of about 15°, 30° and 45°. The optical transmittances of each deflector are also simulated and the transmittances are 88.2%, 86.8% and 71.3% for 15°, 30° and 45° at wavelength of 450 nm; 86.7%, 86.4%, 69.7% for 15°, 30° and 45° at wavelengths of 532 nm and 89.3%, 80.6%, 62.0% for 15°, 30° and 45° at the wavelength of 633 nm. The average transmittance is over 80% and the designed deflectors show low-loss performance with expectation.

Generalized Snell's law and Huygens-Fresnel principle can help to explain the properties of our deflectors. The propagation of the light with phase discontinuities follows the generalized Snell's law [3, 32]:

$$\sin(\theta_r)n_i - \sin(\theta_i)n_i = \frac{\lambda_0}{2\pi}\frac{\mathrm{d}\Phi}{\mathrm{d}x} \quad \text{and}$$

$$\sin(\theta_t)n_t - \sin(\theta_i)n_i = \frac{\lambda_0}{2\pi}\frac{\mathrm{d}\Phi}{\mathrm{d}x},$$

where θ_i, θ_r and θ_t are practical propagation angles of incident, reflection and refraction, n_i and n_t are the refractive indices of the two media, $\mathrm{d}\Phi$ is the phase discontinuities and $\mathrm{d}x$ is the distance between two crossing points of adjacent light paths. Because of the existence of abrupt phase change at the boundary, in which case $\mathrm{d}\Phi/\mathrm{d}x$ doesn't equal to zero, the light wave appears anomalous refraction and the incident light is bent according to the designed phase. In Huygens-Fresnel principle, as the deflector is illuminated with plane wave, each point of the plane wavefront can be regarded as a point source of spherical secondary wave with designated initial phase and the form of the wave at later time is determined by the sum of these secondary waves. Hence, as a result of superposition of these spherical secondary waves, the plane wave is formulated in the far-field, coinciding with the generalized Snell's law.

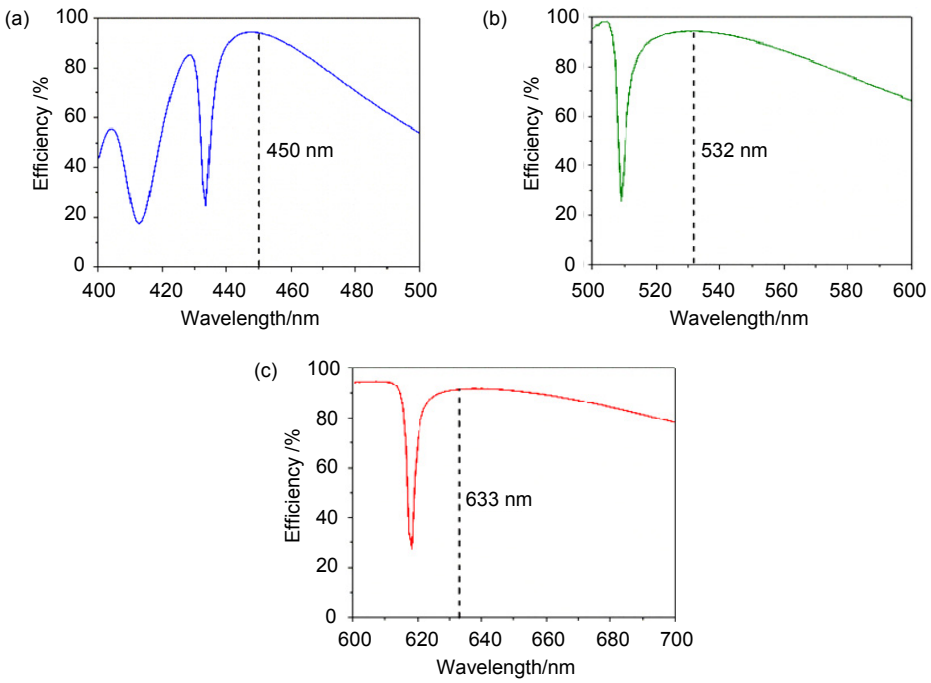

Fig.2 The PCE of the single nanoantenna. (a) *S*=230 nm, *L*=145 nm, *W*=60 nm, *H*=500 nm. (b) *S*=270 nm, *L*=210 nm, *W*=70 nm, *H*=550 nm. (c) *S*=320 nm, *L*=270 nm, *W*=105 nm, *H*=600 nm.

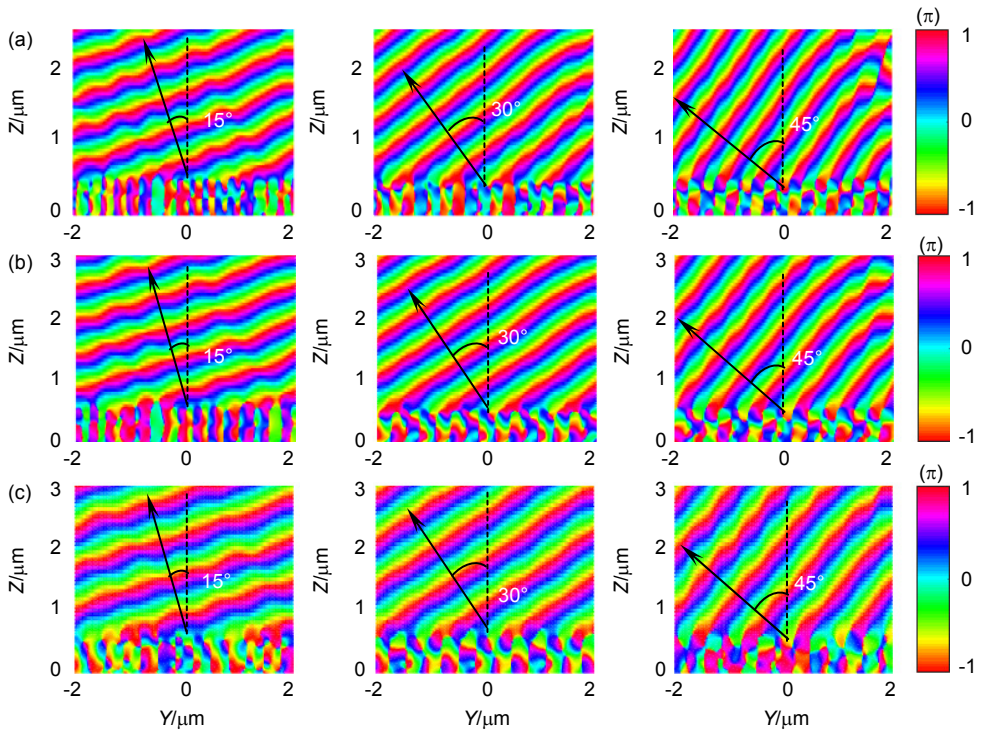

Fig.3 Simulated near-field phase distributions of electric field for 15°, 30° and 45° (from left to right) at the wavelengths of (a) 450 nm with *S*=230 nm, *L*=145 nm, *W*=60 nm, *H*=500 nm, (b) 532 nm with *S*=270 nm, *L*=210 nm, *W*=70 nm, *H*=550 nm, (c) 633 nm *S*=320 nm, *L*=270 nm, *W*=105 nm, *H*=600 nm.

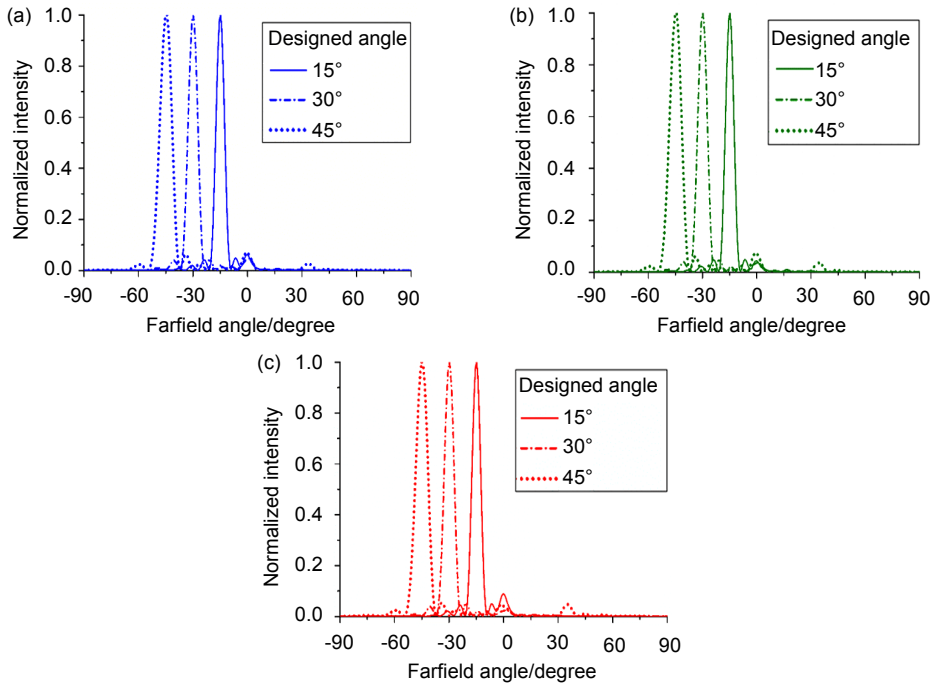

Fig.4 Simulated far-field transmitted power distributions as the functions of angle at the three wavelengths. (a) Blue lines at the wavelength of 450 nm. (b) Green lines at the wavelength of 532nm and (c) red lines at the wavelength of 633 nm. Solid lines, short dash dot lines and short dot lines represent the deflection angles designed for 15°, 30° and 45°, respectively.

4 Conclusions

In summary, one type of visible light beam deflector composed of TiO_2 nanoantennas array is designed and numerically demonstrated to exhibit high transmission efficiency by using phase discontinuities. The performances of various output angles are investigated at three wavelengths corresponding different deflectors. FDTD simulation results show that the proposed deflectors are

in excellent agreement with our theoretical prediction. The phase discontinuity presents a simple and flexible method to design the phase properties of a deflector. The designed deflector is believed to show potentials in the applications of integrated optics.

Acknowledgement

The work is supported in part by the National Natural Science Foundation of China under Grant (61575092). The authors acknowledge support from the Thousand Talents Program for Young Professionals, Collaborative Innovations Center of Advanced Microstructures.

References

1 Xu Ting, Wang Changtao, Du Chunlei, *et al*. Plasmonic beam deflector[J]. *Optics Express*, 2008, **16**(7): 4753−4759.

2 Wang Y, Wang L L, Liu J Q, *et al*. Plasmonic surface-wave bidirectional splitter in different angles of incident light[J]. *Optics Communications*, 2010, **283**(9): 1777−1779.

3 Yu Nanfang, Genevet P, Kats M A, *et al*. Light propagation with phase discontinuities: generalized laws of reflection and refraction[J]. *Science*, 2011, **334**(6054): 333−337.

4 Yu Nanfang, Capasso F. Flat optics with designer metasurfaces[J]. *Nature Materials*, 2014, **13**(2): 139−150.

5 Kildishev A V, Boltasseva A, Shalaev V M. Planar photonics with metasurfaces[J]. *Science*, 2013, **339**(6125): 1232009.

6 Qin Fei, Ding Lu, Zhang Lei, *et al*. Hybrid bilayer plasmonic metasurface efficiently manipulates visible light[J]. *Science Advances*, 2016, **2**(1): e1501168.

7 West P R, Stewart J L, Kildishev A V, *et al*. All-dielectric subwavelength metasurface focusing lens[J]. *Optics Express*, 2014, **22**(21): 26212−26221.

8 Hasman E, Kleiner V, Biener G, *et al*. Polarization dependent focusing lens by use of quantized Pancharatnam-Berry phase diffractive optics[J]. *Applied Physics Letters*, 2003, **82**(3): 328−330.

9 Khorasaninejad M, Aieta F, Kanhaiya P, *et al*. Achromatic metasurface lens at telecommunication wavelengths[J]. *Nano Letters*, 2015, **15**(8): 5358−5362.

10 Khorasaninejad M, Chen W T, Zhu A Y, *et al*. Multispectral chiral imaging with a metalens[J]. *Nano Letters*, 2016, **16**(7): 4595−4600.

11 Ni Xingjie, Kildishev A V, Shalaev V M. Metasurface holograms for visible light[J]. *Nature Communications*, 2013, **4**: 2807.

12 Zheng Guoxing, Mühlenbernd H, Kenney M, *et al*. Metasurface holograms reaching 80% efficiency[J]. *Nature Nanotechnology,* 2015, **10**(4): 308−312.

13 Huang Lingling, Chen Xianzhong, Mühlenbernd H, *et al*. Three-dimensional optical holography using a plasmonic metasurface[J]. *Nature Communications*, 2013, **4**: 2808.

14 Li Xiong, Chen Lianwei, Li Yang, *et al*. Multicolor 3D meta-holography by broadband plasmonic modulation[J]. *Science Advances*, 2016, **2**(11): e1601102.

15 Yu Nanfang, Aieta F, Genevet P, *et al*. A broadband, background-free quarter-wave plate based on plasmonic metasurfaces[J]. *Nano Letters*, 2012, **12**(12): 6328−6333.

16 Chen Weiting, Török P, Foreman M R, *et al*. Integrated plasmonic metasurfaces for spectropolarimetry[J]. *Nanotechnology*, 2016, **27**(22): 224002.

17 Arbabi A, Arbabi E, Kamali S M, *et al*. Miniature optical planar camera based on a wide-angle metasurface doublet corrected for monochromatic aberrations[J]. *Nature Communications*, 2016, **7**: 13682.

18 Ma Xiaoliang, Pu Mingbo, Li Xiong, *et al*. A planar chiral meta-surface for optical vortex generation and focusing[J]. *Scientific Reports*, 2015, **5**: 10365.

19 Aieta F, Kats M A, Genevet P, *et al*. Multiwavelength achromatic metasurfaces by dispersive phase compensation[J]. *Science*, 2015, **347**(6228): 1342−1345.

20 Yang Yuanmu, Wang Wenyi, Moitra P, *et al*. Dielectric meta-reflectarray for broadband linear polarization conversion and optical vortex generation[J]. *Nano Letters*, 2014, **14**(3): 1394−1399.

21 Lin Dianmin, Fan Pengyu, Hasman E, *et al*. Dielectric gradient metasurface optical elements[J]. *Science*, 2014, **345**(6194): 298−302.

22 Sun Shulin, Yang Kuangyu, Wang C M, *et al*. High-efficiency broadband anomalous reflection by gradient meta-surfaces[J]. *Nano Letters*, 2012, **12**(12): 6223−6229.

23 Pors A, Bozhevolnyi S I. Plasmonic metasurfaces for efficient phase control in reflection[J]. *Optics Express*, 2013, **21**(22): 27438−27451.

24 Khorasaninejad M, Chen Weiting, Devlin R C, *et al*. Metalenses at visible wavelengths: diffraction-limited focusing and subwavelength resolution imaging[J]. *Science*, 2016, **352** (6290): 1190−1194.

25 Liu Zhaocheng, Li Zhancheng, Liu Zhe, *et al*. Beam Deflectors: high-performance broadband circularly polarized beam deflector by mirror effect of multinanorod metasurfaces[J]. *Advanced Functional Materials*, 2015, **25**(34): 5567.

26 Su Xiaoqiang, Ouyang Chunmei, Xu Ningning, *et al*. Active metasurface terahertz deflector with phase discontinuities[J]. *Optics Express*, 2015, **23**(21): 27152−27158.

27 Shalaev M I, Sun Jingbo, Tsukernik A, *et al*. High-efficiency all-dielectric metasurfaces for ultracompact beam manipulation in transmission mode[J]. *Nano Letters*, 2015, **15**(9): 6261−6266.

28 Khorasaninejad M, Crozier K B. Silicon nanofin grating as a miniature chirality-distinguishing beam-splitter[J]. *Nature Communications*, 2014, **5**: 5386.

29 Ding Xumin, Monticone F, Zhang Kuang, *et al*. Ultrathin pancharatnam-berry metasurface with maximal cross-polarization efficiency[J]. *Advanced Materials*, 2015, **27**(7): 1195−1200.

30 Zhao Wenyu, Jiang Huan, Liu Bingyi, *et al*. High-efficiency beam manipulation combining geometric phase with anisotropic Huygens surface[J]. *Applied Physics Letters*, 2016, **108**(18): 181102.

31 DeVore J R. Refractive indices of rutile and sphalerite[J]. *Journal of the Optical Society of America*, 1951, **41**(6): 416−419.

32 Zhang Xueqian, Tian Zhen, Yue Weisheng, *et al*. Broadband terahertz wave deflection based on C-shape complex metamaterials with phase discontinuities[J]. *Advanced Materials*, 2013, **25**(33): 4567−4572.